REPORT DOCUMENTATION PAGE

Form Approved
OMB No. 0704-0188

1. REPORT DATE *(DD-MM-YYYY)*	**2. REPORT TYPE**	**3. DATES COVERED** *(From - To)*
November 2015	Technical Paper	January 2014-February 2015

4. TITLE AND SUBTITLE
Health Monitoring and Diagnosis of Solid Rocket Motors with Bore Cracks

5a. CONTRACT NUMBER

5b. GRANT NUMBER

5c. PROGRAM ELEMENT NUMBER

6. AUTHOR(S)
Anhduong Q. Le, L. Z. Sun, and Timothy C. Miller

5d. PROJECT NUMBER

5e. TASK NUMBER

5f. WORK UNIT NUMBER
Q16H

7. PERFORMING ORGANIZATION NAME(S) AND ADDRESS(ES)

Air Force Research Laboratory (AFMC)
AFRL/ RQRP
10 E Saturn Blvd
Edwards AFB, CA 93524

8. PERFORMING ORGANIZATION REPORT NO.

9. SPONSORING / MONITORING AGENCY NAME(S) AND ADDRESS(ES)

Air Force Research Laboratory (AFMC)
AFRL/RQR
5 Pollux Drive
Edwards AFB, CA 93524-7048

10. SPONSOR/MONITOR'S ACRONYM(S)

11. SPONSOR/MONITOR'S REPORT NUMBER(S)
AFRL-RQ-ED-TP-2015-003

12. DISTRIBUTION / AVAILABILITY STATEMENT
Approved for public release; distribution unlimited

13. SUPPLEMENTARY NOTES
For publication in Structural Health Monitoring (November 2015)
PA Case Number: #15060; Clearance Date: 5 February 2015

14. ABSTRACT
A finite-element-based computational model is used to investigate the effects of bore cracking on the changes in stress distributions along the bondline of solid rocket motors at various storage temperatures. Capabilities of a rocket motor health monitoring system are assessed based on the assumption that the proposed stress sensors are evenly distributed along the circumference of the inside of the motor case. A quantitative relationship is obtained between the crack depth and the sensor data to inversely estimate the size of bore cracks in the motor. It is shown that the proposed type of sensing system can detect critical bore cracks in solid rocket motors.

15. SUBJECT TERMS
structural health monitoring (SHM) · structural integrity · damage detection · stress sensor · temperature sensor · rocket propellant · solid rocket motor (SRM)

16. SECURITY CLASSIFICATION OF:			**17. LIMITATION OF ABSTRACT**	**18. NUMBER OF PAGES**	**19a. NAME OF RESPONSIBLE PERSON**
a. REPORT	**b. ABSTRACT**	**c. THIS PAGE**			N/A
Unclassified	**Unclassified**	**Unclassified**	SAR	13	**19b. TELEPHONE NO** *(include area code)* N/A

Standard Form 298 (Rev. 8-98)
Prescribed by ANSI Std. 239.18

Health Monitoring and Diagnosis of Solid Rocket Motors with Bore Cracks

Anhduong Q. Le[1], L. Z. Sun[1], and Timothy C. Miller[2,*]

[1]*University of California, Irvine, CA 92697-2175*
[2]*Air Force Research Laboratory, Edwards AFB, CA 93524*

A finite-element-based computational model is used to investigate the effects of bore cracking on the changes in stress distributions along the bondline of solid rocket motors at various storage temperatures. Capabilities of a rocket motor health monitoring system are assessed based on the assumption that the proposed stress sensors are evenly distributed along the circumference of the inside of the motor case. A quantitative relationship is obtained between the crack depth and the sensor data to inversely estimate the size of bore cracks in the motor. It is shown that the proposed type of sensing system can detect critical bore cracks in solid rocket motors.

Keywords: structural health monitoring (SHM) · structural integrity · damage detection · stress sensor · temperature sensor · rocket propellant · solid rocket motor (SRM)

1 Introduction

Structural health monitoring is of significant interest for the safety and reliability of solid rocket motors (SRMs) [1-3]. The ability to detect damage in SRMs will help enable timely, accurate, and reliable assessment of structural integrity, yielding great cost savings and preventing catastrophic structural failures [4]. Because SRMs are cooled from the cure temperature to an ambient temperature, residual stress fields persist in the grain throughout its life, and as a result, SRMs can develop flaws that can cause catastrophic failure on ignition. There are three primary failure mechanisms: propellant aging in the grain [5-7], cracking near the bore [8-10], and delamination at the interfaces between the propellant, insulation, and case [5, 11]. Bore cracking occurs typically at the midplane of the motor and grows radially towards the case while simultaneously extending longitudinally towards the ends of the motor. While fracture mechanics based quantitative investigations are available for stress and strain distributions in motors due to bore cracks, little has been done on the inverse problem of detecting bore-cracks in SRMs in the literature.

In this paper, we use finite element methods to investigate the effects of bore cracks on the radial stress fields at the bondline during the cooling process of a solid rocket motor. With the assumption of stress sensors evenly distributed along the inner wall of the case, the relationship between the bore crack depth, the number of sensors, and the required sensor accuracy is established. In addition, a quantitative mapping is obtained between the crack depth and the sensor data so that crack depth can be inversely estimated. It is shown that the proposed framework can successfully detect bore cracking in solid rocket motors.

* Author to whom correspondence should be addressed. E-mail: timothy.miller.26@us.af.mil; Fax: 661-275-5435; Phone: 661-275-5323

2 Methodology

The solid rocket motor we chose to model is a simplified version of a center-perforated motor, as shown in Figure 1. Because of symmetry, only half of the cross section is modeled. The inner and outer grain diameters are 203.2 mm and 406.4 mm, respectively. The thickness of the insulation and case are 2.54 and 3.175 mm, respectively. The propellant is a typical composite grain of hydroxyl-terminated polybutadiene/ammonium perchlorate (HTPB/AP). The insulation layer is ethylene propylene diene monomer (EPDM). The temperature-dependent mechanical properties of HTPB/AP and EPDM were obtained from in-house testing at the U.S. Air Force Research Laboratory (Edwards Air Force Base, CA). The motor case is assumed to be a filament-wound graphite-epoxy motor. A simplified symmetric layup with winding angles of $(0^\circ/90^\circ/\pm 45^\circ)_s$ is assumed and modeled with quasi-isotropic thermal-elastic responses (Young's modulus is 55.9 GPa, Poisson's ratio is 0.30, and the coefficient of thermal expansion is 2.16×10^{-6} K^{-1}) [12].

In an attempt to improve the failure tendencies of SRMs, designers have incorporated stress-relieving flaps and boots near the ends of the propellant grain. However, since damage in composite propellants and related flaw development are favored in regions of high stress triaxiality, bore cracks can still develop near the center of the motor. In this work, it is assumed that a bore crack typically develops first at the motor midplane and then propagates longitudinally towards both ends of the motor. Because of the bore crack proclivity for nucleation at the midplane, the corresponding two-dimensional plane-strain problem can be analyzed using the finite element method to investigate the effect of a bore crack on the local stress distribution. The plane-strain assumption is warranted by the length-to-diameter ratio of most rocket motors. The analysis is performed using the commercially available finite element software package ABAQUS. Five bore crack cases are considered with different crack sizes: 8.0, 12.7, 25.4, 38.1, and 50.8 mm (with a web thickness of 101.6 mm, the corresponding crack depths normalized by the web thickness are 0.08, 0.125, 0.25, 0.375, and 0.50). All of the models are subjected to slow temperature cooling from the cure temperature to a service temperature. With a stress-free cure temperature of 58˚C, an additional 2˚C in temperature drop to account for cure shrinkage effects, and a final service temperature of -40˚C, the total effective temperature drop used is 100˚C.

Figure 2 shows a typical mesh with a crack extending 38.1 mm from the bore surface into the grain. The mesh is highly focused at the crack tip to give good resolution of the near-tip stress fields. There were 31750 nodes and 6287 elements used in this mesh; models for the other crack depths have a similar level of refinement. The elements were quadratic isoparametric hybrid elements with reduced-order integration. The hybrid elements available with the ABAQUS software incorporate pressure as an independent variable to help prevent computational problems with incompressible or nearly incompressible materials. Symmetry boundary conditions constrain horizontal motion along the left edge of the models (see Figure 1) except on the crack faces, and a single vertical nodal restraint prevents rigid body motion. The radial, hoop, and shear stresses at the propellant/insulation surface were determined for temperature drops from 60˚C to -40˚C (cooling takes place in a quasistatic fashion with 10˚C increments).

3 Results and Discussion

Figure 3 shows the Dual Bond Stress and Temperature (DBST) sensor that is proposed for health monitoring of solid rocket motors [11, 13]. These sensors measure both radial stress and temperature near the case wall. The sensors are mounted to the case wall during the manufacturing process. In this paper, we use an assumed accuracy for a difference between two sensor readings of 10 kPa. This assumed value is based on our previous experience with the sensors over many years of testing, and is an upper bound for sensor accuracy. More details on the accuracy of these sensors are given in Section 4. Since the sensors measure radial stresses near the case wall, we focused mostly on these stresses, although hoop stresses are consistently higher in magnitude and could be another means to detect anomalies in motors. Figure 4 shows typical finite element model contour plots of radial, hoop, and shear stresses in a flawed propellant grain (the case and insulation layer are not shown for clarity). The plots shown here are for a bore crack size of 38.1 mm at -40˚C. It is demonstrated that the magnitudes of radial and hoop stresses are in the same order while shear stresses are much less than those normal stresses. A stress singularity occurs at the crack tip for all three stress fields.

Figure 5 further shows the radial stresses near the case wall in an "unwrapped" fashion – in this graph, a value of $\phi = 0°$ indicates the stresses immediately over the flaw, and $\phi = 180°$ indicates the stresses diametrically opposite to the flaw. Graphs for all of the flaw depths are shown and can be compared to the baseline value of 855 kPa. This graph can be interpreted as follows: cooling an uncracked motor by 100 °C causes a radial stress of 855 kPa to be experienced near the case wall. However, as a flaw develops, this baseline stress value is perturbed near the flaw, with points remote from the defect approaching the baseline value. As the flaw grows, the absolute values of the perturbations increase, as does the range over which they take place. These perturbations affect the sensors and can be used to analyze the health of the motor.

For example, assume that a four-sensor system is employed; so that four sensors are distributed evenly along the case wall in a ring at the motor midplane (see Figure 1). The maximum and minimum values of the four sensor readings are compared for various positions of the sensor set (the position of the sensor set is characterized by θ in Figure 1). The least optimal location (corresponding to the smallest value of these differences) can be compared with sensor accuracy for various defect sizes – for a given defect size, if this difference is larger than the sensor accuracy, then the sensor data can be used to detect the flaw. In Figure 6, data for a crack length 12.7 mm is shown. The smallest difference between maximum and minimum stress values of the four sensors takes place if $\theta = 10^{\circ}$ (or 80°), and this difference is 18.6 kPa. In other words, no matter where the sensors are located, the difference between the maximum and the minimum values of the four sensor readings is always larger than 18.6 kPa. For the sensors currently being considered, the stress values are accurate to ±10 kPa [11, 13]. The implication is that by comparing the four sensor values, defects with crack length 12.7 mm in this solid rocket motor could be detected with 100% probability.

Similar analyses were conducted for three-sensor and six-sensor systems. For the crack depth of 12.7 mm, the differences between the maximum and minimum readings at the least-optimal locations were 5.18 kPa and 25.5 kPa respectively, for the three-sensor system and the six-sensor system. By performing similar analyses for all of the flaw sizes, a set of curves are constructed as shown in Figure 7, demonstrating that increasing the number of sensors improves flaw

detectability. For example with only three sensors, the detectable bore crack depth is only 18.8 mm, while with a four-sensor system it is 9.0 mm, and with the six-sensor system it is only 7.6 mm. Such an approach can be used with other motor geometries to produce similar curves, which can then be applied to assess the effectiveness of health monitoring systems with respect to detection of bore cracks.

3.1 Acquiring Data at Different Temperatures

Until now, we have assumed that the health monitoring data was acquired by cooling the motor slowly to a service temperature of -40˚C. Although giving the biggest response, the sensors can still detect defects at less extreme temperatures. To examine the effect of service temperature on flaw detectability, a four-sensor system is assumed to be cooled from the stress free temperature to final temperatures of 20˚C, 0˚C, -20˚C, and -40˚C with the crack length in this case being 12.7 mm. The analysis is summarized in Figure 8. It is shown that the detectability is enhanced by taking sensor readings at lower temperatures. With four sensors, the crack length 12.7 mm can be detected with 100% probability at or below -20˚C. Above this temperature, the probability of detection is reduced but still quite high, as is shown later – see the Section 3.3. Of course, for a slightly larger flaw, the entire curve would be shifted upwards – a family of curves could be generated from the finite element data. Using such data, a test temperature could be selected that ensured detection of critical flaws while still minimizing cooling requirements for the test.

3.2 Detectability when One Sensor Fails

The health monitoring system capability can be enhanced with more sensors embedded, and the cost of these sensors is only a small fraction of the cost of the motor. However, using an excessive number of sensors can lead to a complicated, expensive system with excessive data storage and analysis requirements. The question is that what the best number of sensors is to use. Until this point, our discussion has assumed that all sensors in the system work for the duration of the motor life. However, results can be determined if we assume, say, that one random sensor in a four-sensor system has failed. It is interesting to investigate the four-sensor system in terms of detectability of a 12.7 mm deep bore crack when a random sensor fails. An analysis of the perturbed radial stress data from the finite element model shows that in the event of a random failure of one sensor in a four-sensor system, the stress differences between the three remaining sensors will still detect a defect over 80% of the time (assuming 10 kPa sensor accuracy).

3.3 Percentage of Detectability

Previously, when we analyzed data in the “least-optimal location,” it gave a conservative estimate of health monitoring system performance. However, this approach ignores most of the data – it is possible to use the entire data set (for example, the entire curve in Figure 6, as opposed to its minimum) to determine a probability of detection for a fleet of motors. Some flaws will be oriented so that the sensors can detect the flaw, but some will not. Probability of detection arises from a comparison of a curve like that in Figure 6 with the sensor accuracy level. This concept was employed to analyze three-, four-, and six-sensor systems in this section at an assumed test temperature of -40 ˚C and with an assumed sensor accuracy of 10 kPa. Figure 9 shows the results of these analyses. Obviously very small cracks will be undetectable for all of the sensor configurations (we found, for example, that a 4-mm-deep flaw was undetectable). However, for the flaw sizes shown here, the various systems performed fairly well – for

example, for a 12.7-mm-deep bore crack, the three-sensor system had 88% probability of detection, and the four- and six-sensor systems had 100% probability (this is the middle set of bars in Figure 9). Analyses of finite element data such as shown in Figure 9 can help motor analysts decide how many sensors to use in a given situation.

3.4 Estimation of Crack Length

With the in-depth analysis of finite element simulation, we have found a method to estimate the depth of the bore crack using just the sensor data. The following method is proposed by the authors to estimate the crack length – in this case, we illustrate it with a four-sensor system and a temperature drop of 100˚C. This method focuses on the difference between the maximum and minimum values of the sensor readings (i.e., the range of the sensor data).

For each crack location relative to the sensors, a set of data is produced. If the full range of crack locations is considered and the sensors readings are arranged in decreasing order: R_1, R_2, R_3, and R_4 for all of this finite element data and tabulated, a curve can be constructed in Figure 10, showing the range (scattered points) of values ($R_1 - R_4$) as a function of crack length. The solid lines in the figure represent the boundaries of the locus of ($R_1 - R_4$) for all crack lengths considered (0 to 38.1 mm). Therefore, for a given crack length, the values of ($R_1 - R_4$) lie within a defined envelope. With no crack (x = 0 in Figure 10), R_1, R_2, R_3, and R_4 are always equal, thus the stress difference is zero – but the value of R_1-R_4 increases with crack length. To use the graph, the value of ($R_1 - R_4$) is obtained from sensor readings and is located on the vertical axis, and then a horizontal line is drawn. The intersection of this horizontal line with the bounding curves shown in Figure 10 gives the lower and upper estimates of the bore crack depth. For example, if the two stress readings R_1 and R_4 differ by 20 kPa, then the corresponding crack length is between 10 mm and 14 mm.

4 Conclusions

Health monitoring sensor data can be used to detect bore cracks in solid rocket motors. The proposed health monitoring system employs combined stress and temperature sensors to measure radial stresses experienced by the propellant grain because of cooling from the stress-free temperature. An unflawed motor will have sensors with very similar readings at all test temperatures; however, as a bore crack develops, it will perturb the stress field and reveal itself through variations in the sensor data. In this paper, we have described in detail how an analysis of finite element data can determine the effectiveness of such a sensor system, and can also aid in the design of such a system. Our analysis, using a typical motor geometry and sensor accuracy show that (i) the sensors should be able to detect critically sized bore cracks, (ii) the detection capabilities depend on the number of sensors and the test temperature, (iii) percent of detection can be assessed from study of the finite element data, (iv) degradation of one of the sensors does not destroy the capability of the system to detect cracks, and (v) an inverse method has been proposed to estimate the bore crack depth based solely on sensor data. Future work on these sensor systems will involve experimental work to validate these relationships, as well as an investigation of the response of the system to other flaw types such as interfacial debonds.

Acknowledgements

This work was made possible by the U.S. Air Force Research Lab at Edwards Air Force Base (AFRL), which supported the Air Force Summer Faculty Fellowship Program (SFFP) administered by the American Society for Engineering Education (ASEE). The authors gratefully acknowledge technical assistance from Jim Buswell and Herb Chelner of Micron Instruments in regards to the dual bond stress and temperature (DBST) sensors and Greg Yandek of AFRL/RQRP for the data collection of EPDM insulation material.

References

1. Ruderman, G.A. (2005). Health management and strategy for Air Force missiles, Report AFRL-PR-ED-TP-2005-272, U.S. Air Force Research Laboratory, Edwards Air Force Base, CA.

2. Little, R.R., Chelner, H., and Buswell, H.J. (2006). Development, testing, and application of embedded sensors for solid rocket motor health monitoring. In: *Proceedings of 37th Annual Conference of Fraunhofer-Institute for Chemical Technology (ICT)*, Karlsruhe, Germany, 1-12.

3. McDonald, A.J. (2010). Solid rocket motor failure. In: *Encyclopedia of Aerospace Engineering, Vol. 2*, Wiley and Sons, NY, 1123-1129.

4. Ozupek, S. (2010). Computational procedure for the life assessment of solid rocket motors. *AIAA Journal of Spacecraft and Rockets, 47(4)*, 639-648.

5. Reeling Brouwer, G., Pfiffer, A., and Bancallari, L. (2011). Development and deployment of diagnostic prognostic tactical solid rocket motor demonstrator. In: *47th AIAA/ASME/SAE/ASEE Joint Propulsion Conference and Exhibit*, San Diego, CA, 1-11.

6. Iqbal, M.M., Liang, W. (2006). Modeling the moisture effects of solid ingredients on composite propellant properties. *Aerospace Science and Technology, 10(8),* 695-699.

7. Cerri, S., Bohn, M.A., Menke, K., Galfetti, L. (2009). Ageing behaviour of HTPB rocket propellant formulations. *Central European Journal of Energetic Materials, 6(2)*, 149-165.

8. Ho, S.-Y., Care, G. (1998). Modified fracture mechanics approach in structural analysis of solid-rocket motors. *AIAA Journal of Propulsion and Power, 14(4)*, 409-415.

9. Wong, F.C. (2003). Pseudodomain fracture analysis of instrumented analog rocket motors. *AIAA Journal of Spacecraft and Rockets, 40(1)*, 92-100.

10. Tussiwand, G.S., Oley, D., Besser, H.-L., Weterings, F.P., Brouwer, G.C.R. (2007). Application of embedded sensor technology to a full-scale experimental nozzleless rocket motor. In *Proceedings of the 43rd AIAA/ASME/SAE/ASEE Joint Propulsion Conference and Exhibit*, Cincinnati, OH, 1-18.

11. Le, A.Q., Sun, L.Z., Miller, T.C. (2013). Detectability of delaminations in solid rocket motors with embedded stress sensors. *AIAA Journal of Propulsion and Power* (publication pending).

12. Delmonte, J. (1981). *Technology of Carbon and Graphite Fiber Composites.* Van Nostrand Reinhold Company, NY.

13. Chelner, H. (2003). Embedded sensor technology for solid rocket motor health monitoring. SBIR Phase I Final Report, Contract No. DAAH01-02-R099, U.S. Army Aviation and Missile Command, Redstone Arsenal, Huntsville, AL.

Figures

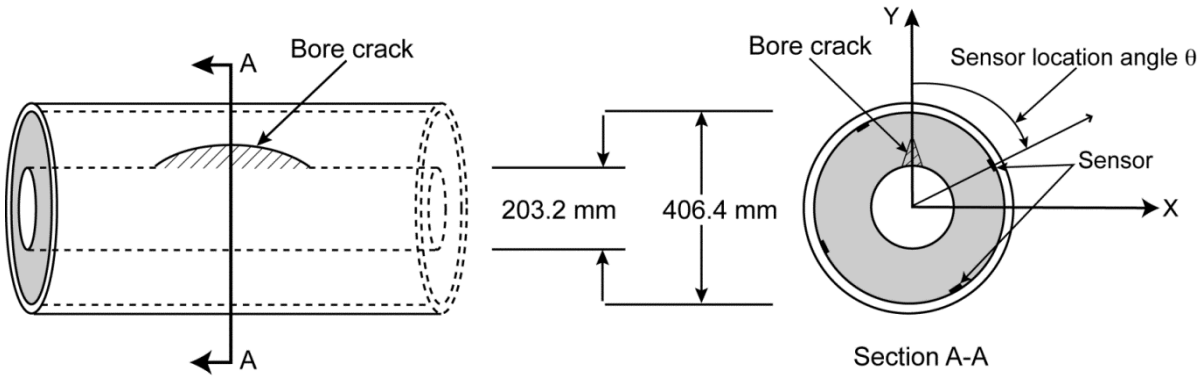

Figure 1 Schematic of rocket motor with bore crack centered on the motor midplane (section A-A).

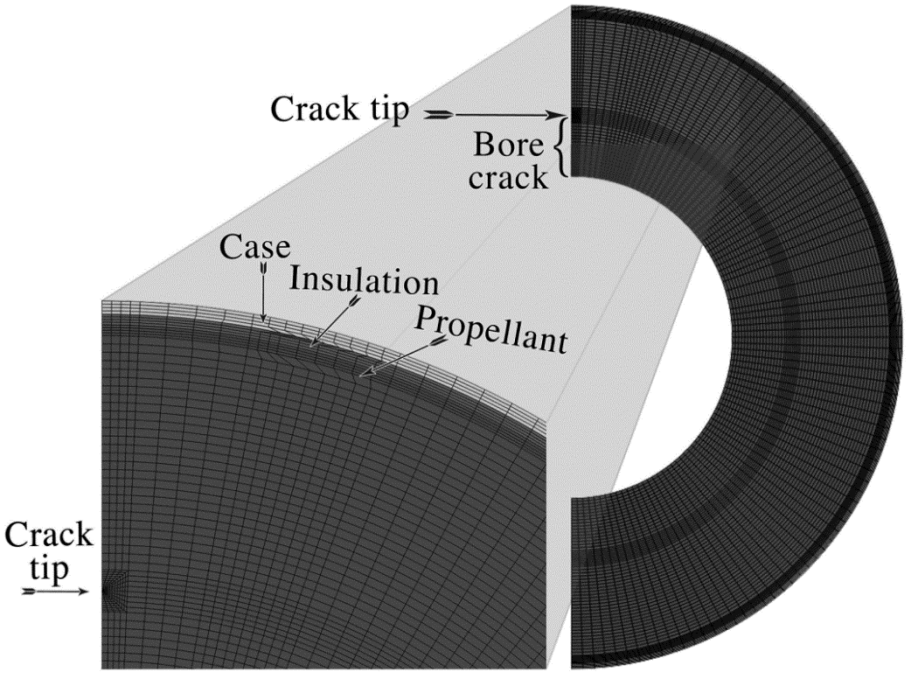

Figure 2 A typical finite element mesh used for analysis of the sensor system.

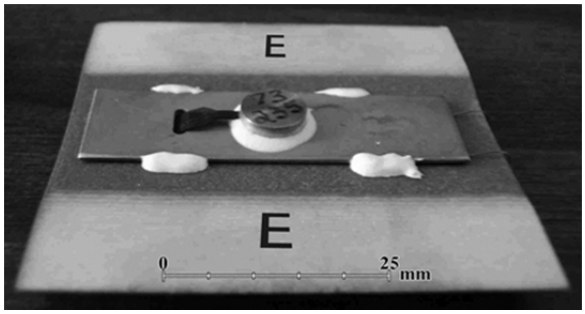

Figure 3 A wireless stress and temperature sensor showing the diaphragm and the mounting shim.

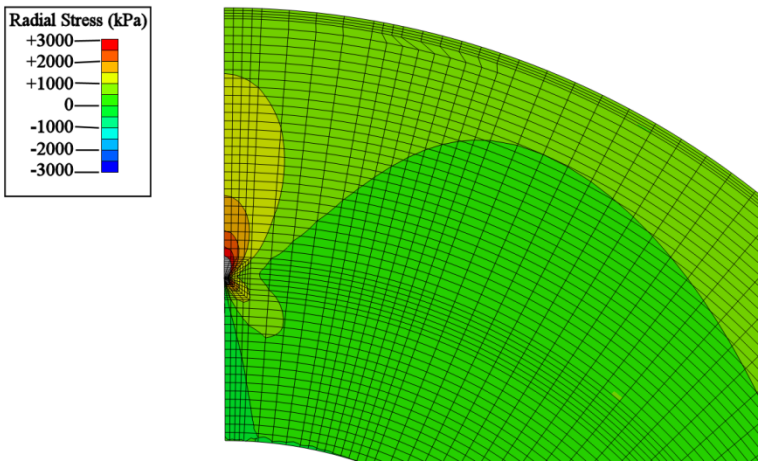

(a)

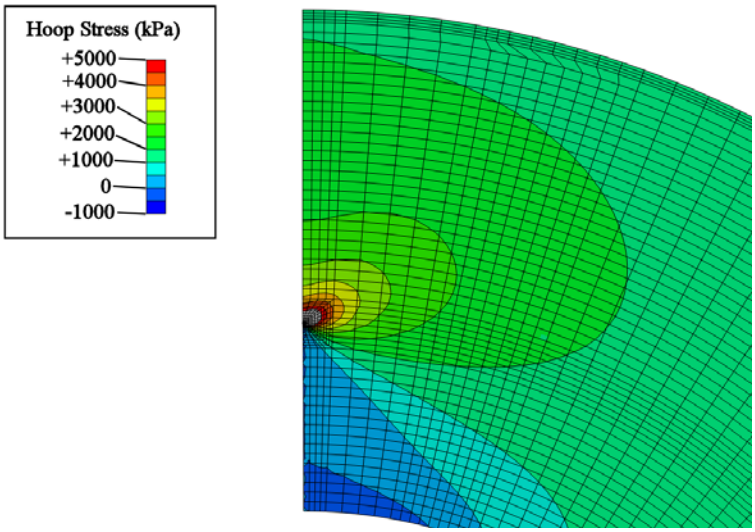

(b)

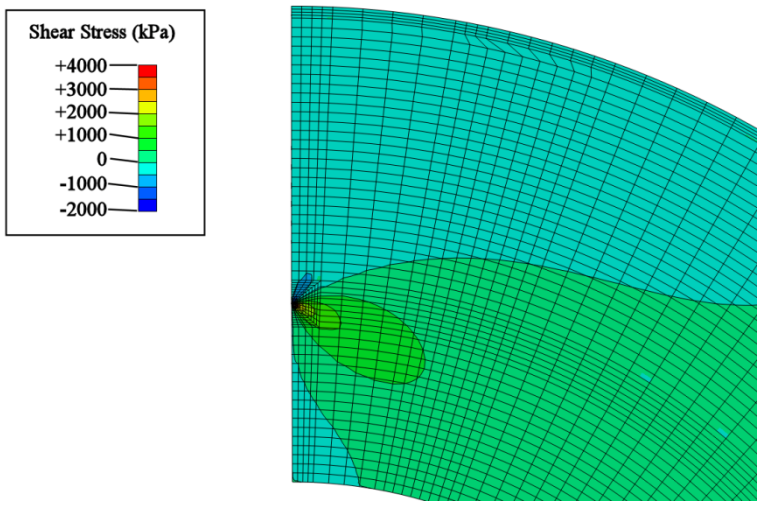

(c)

Figure 4 Contour plots of various stress components in a flawed propellant grain (the case and insulation material are not shown for clarity).

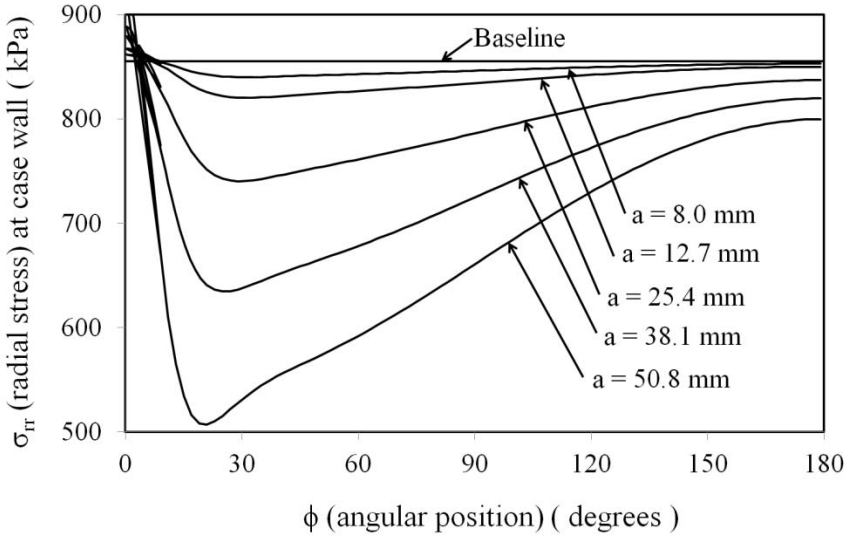

Figure 5 Radial stresses along the edge of the propellant grain for various crack lengths.

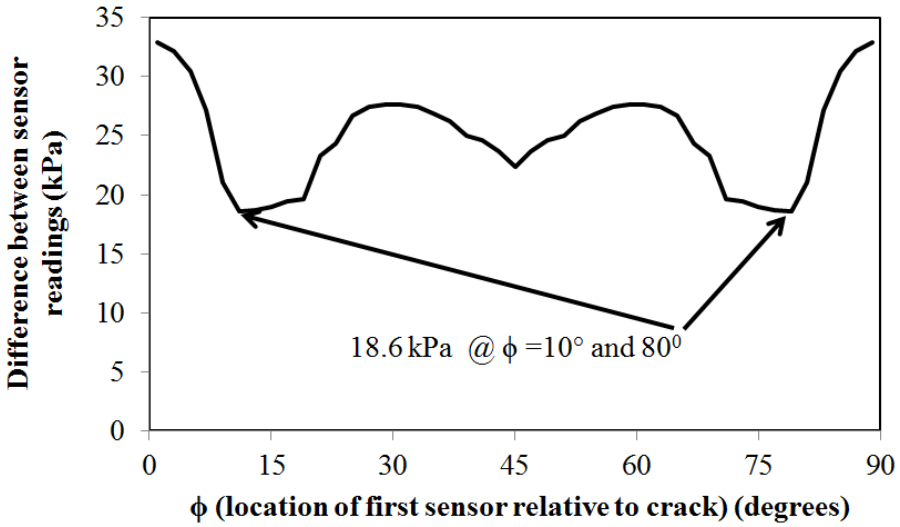

Figure 6 Differences among the four stress sensor readings as a function of position. The data shown is for a 12.7 mm crack length at the lowest temperature (-40˚C).

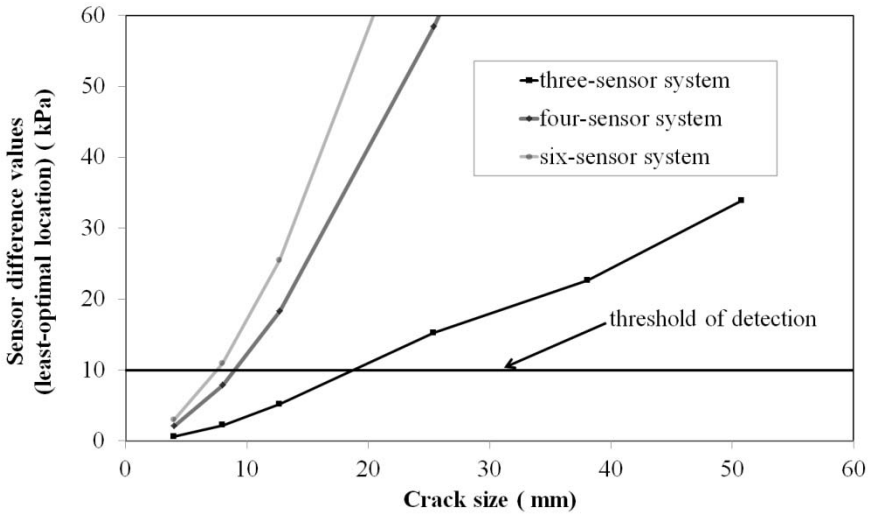

Figure 7 Relationship between stress differences (in the least optimal location) and detectable flaw depths using various numbers of sensors.

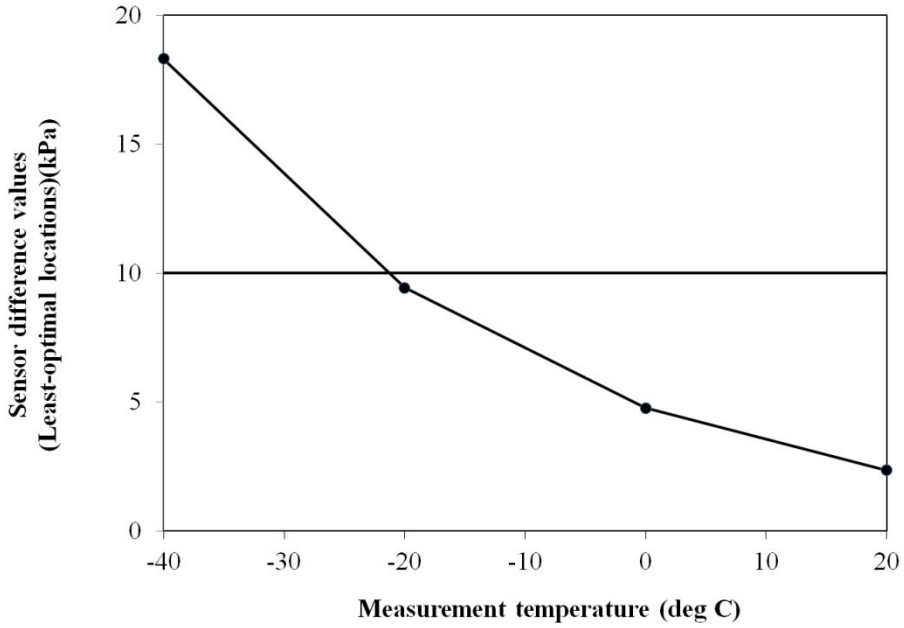

Figure 8 Stress differences in a four-sensor system at the least-optimal location at various temperatures.

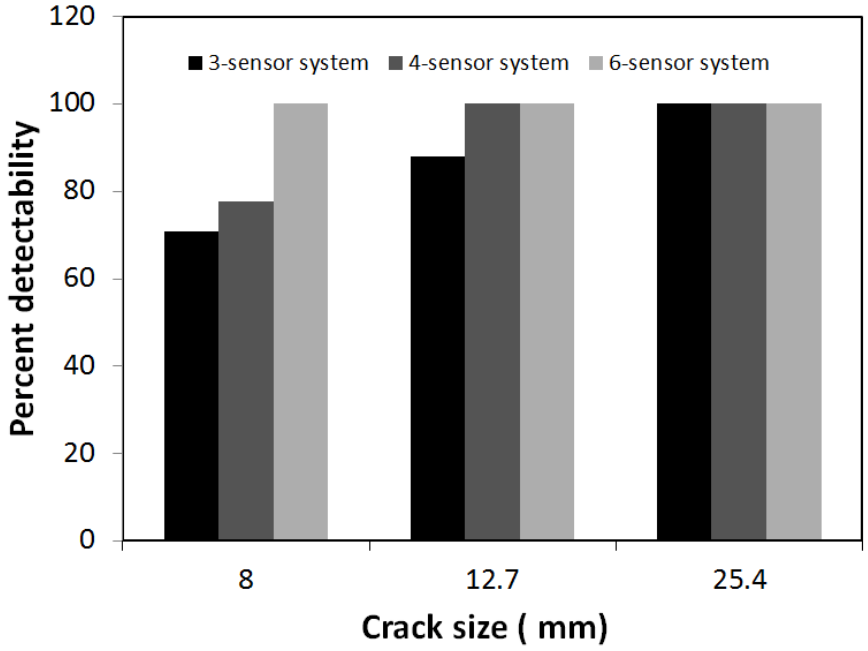

Figure 9 Detectability of flaws for the two proposed methods of analyzing data.

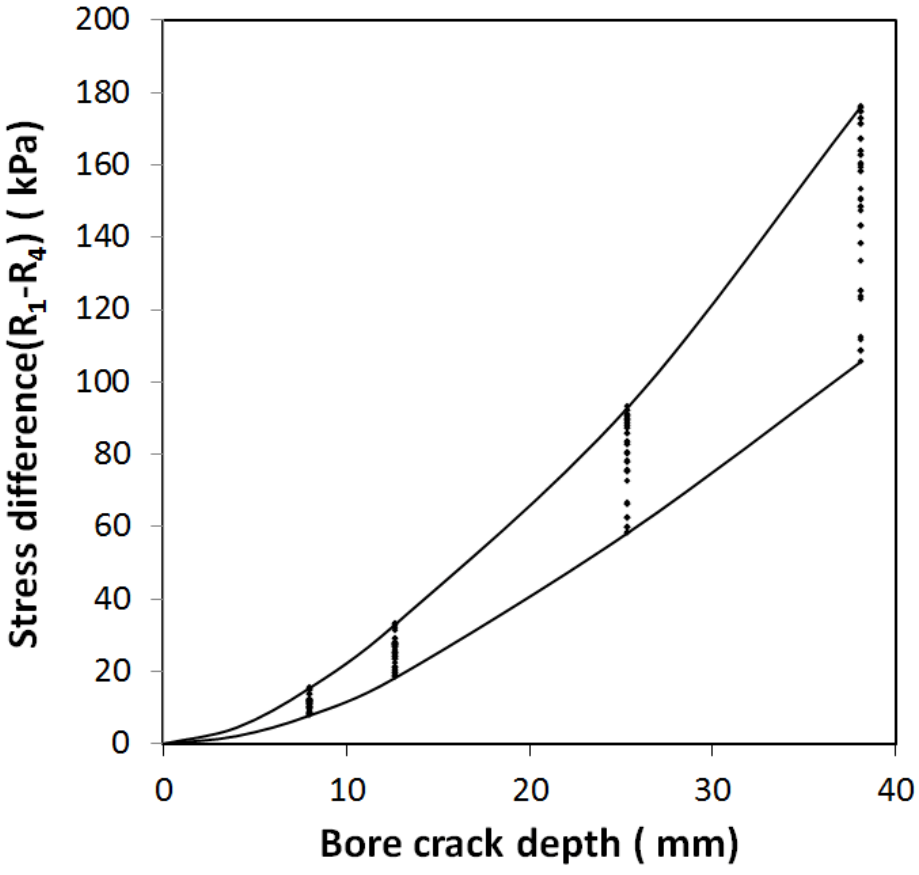

Figure 10 A method for determining the extent of the flaw using four-sensor system data.